ISSN 1392-1207. MECHANIKA. Vol. 29, No. 6, 2023: 462–475

Modeling and Analysis of Flexible Deployable Structure with Scissor-Like Elements Using a Novel Non-Locking Beam Element

Bo LI*, Qi'an PENG, Sanmin WANG*, Jihong ZHU*, Gantes J. CHARIS*****
**School of Mechanical Engineering, Northwestern Polytechnical University, Xi'an 710072, China,*
E-mail: yunfenglibo@126.com
***Institute of Electronic Engineering, China Academy of Engineering Physics, Mianyang, 6219001, China,*
E-mail: pengqian0530@foxmail.com (Corresponding author)
****Institute of Steel Structures, School of Civil Engineering, National Technical University of Athens, 9 Heroon Polytechneiou, Zografou GR-15780, Greece*
https://doi.org/10.5755/j02.mech.33610

1. Introduction

Deployable structure is a new type of aerospace structure born in the late 1960s with the development of aerospace science and technology, which is in a folded state during launch, and is fixed in the payload compartment of the vehicle with the smallest volume. After launching into orbit, the ground command center will control the deployable structure to expand gradually according to the design requirements, becoming a large and complex aerospace structure, and then lock it and keep it in operation [1]. After more than 60 years of development, in order to meet the demanding space environment conditions and special mission needs, a variety of colorful and novel deployable structures have been born, such as the unit frame deployable antenna, rib supported deployable antenna, and other deployable structural forms, such as inflatable antenna, ring column antenna, integral deployable antenna, etc. [2 – 4].There are many types of elements that constitute deployable mechanisms, including scissor element [5], parallelogram element [6], Brickard [7] and Bennet linkage [8]. According to the needs of the project, the unit mechanism can form deployable mechanisms with different configurations through a certain array combination, such as solar panels, radar antenna arrays, etc. Among them, the scissor deployable structure assembled by the scissor element is widely used in the plane extension arm [9], the quadrilateral section extension arm [10], the spherical grid system [11], and the flexible and semi-rigid complex deployable mechanism composed of these basic forms or other structural elements, because of its large shrinkage, reliable deployment, high precision and high stiffness.

Due to the continuous development of space mechanisms towards light weight and high precision, some flexible components with lightweight and large flexibility characteristics are widely used in such mechanisms. The coupling between elastic deformation and large range motion of flexible components will have a great impact on the dynamic characteristics of the mechanism. On the other hand, with the continuous exploration of space science, space technology and space applications by major aerospace countries, deployable structures with deployment/contraction characteristics have been widely used, especially large deployable structures with a characteristic size of 10 m-100 m [12]. With the gradual implementation of major aerospace projects, this type of deployable structure presents some basic characteristics: 1. It shrinks in a small space before launch, and deploys actively after entering orbit. The coupling of structure deployment and spacecraft body motion has an impact on spacecraft attitude; 2. The structure has light weight, large flexibility, small damping and much joint clearance, which easily leads to complex nonlinear dynamic characteristics; 3. The requirement of development precision is high, and the development environment is complex. In the technical development of deployable structures, it is not only necessary to study high-performance aerospace materials and reliable design, but also to pay more attention to the dynamic deployment process of such mechanisms, especially the high-dimensional nonlinear dynamics problems caused by structural deployment, structural flexibility, structural clearance, etc. Therefore, in order to ensure the precise deployment of deployable structure on orbit, it is particularly important to analyze the deployment dynamics of such space articulated mechanisms.

At present, the research on the dynamic characteristics of deployable structure is mainly carried out from the following aspects: 1. The nonlinearity of hinges. Hinge is an important component of aerospace hinge structure, and also an important source of its nonlinearity. Due to processing error, assembly, friction and wear, there is inevitably a clearance in the hinge, and the resulting joint collision, friction and wear lead to asynchronous deployment of the deployable structure. Focusing on the contact impact inside the clearance hinge, Li et al [13] used Monte Carlo method to reveal the influence of random parameters on the motion accuracy and dynamic performance of the spatial deployable structure based on the continuous contact force model. Bai et al [14] studied the dynamic modeling and analysis process of space satellite antenna system with clearance, and pointed out that the influence of axial clearance on satellite antenna system cannot be ignored. Li et al [15] studied the dynamic characteristics of the scissor deployable structure in the process of deployment motion using the Lagrangian method. At the same time, the geometric constraint method was used to control the contact collision phenomenon within the joint to ensure the deployment accuracy and improve the deployment stability. Focusing on the friction and wear in the clearance hinge, Li et al [16] took the solar cell array system as an example to discuss the dynamic response and wear characteristics of the multi-body system with joint clearance and solid coating, and revealed the influence of coating, material and recovery coefficient on the impact performance of rigid system and rigid flexible coupling system. Considering the change of contact surface, Li et al [17] used an improved

nonlinear contact force model suitable for complex contact conditions to evaluate the internal force of joints, and discussed the friction effect between interconnects using the LuGre model. Next, the developed contact force was integrated into the Archard model, and the crank slider mechanism with multiple clearances was numerically simulated to prove the efficiency of the dynamic program used in the whole work. Patil et al [18] proposed a four degree of freedom model and modeled the contact between rolling elements and raceways based on Hertz contact theory. The results show that the vibration level of the bearing increases with the increase of the bearing clearance. Considering the influence of contact stiffness, Zhu et al [19] calculated the contact pressure distribution and contact surface wear respectively using the asymmetric Winkler surface model and Archard wear theory, and obtained the dynamic wear trend of the clearance joint. Focusing on the internal lubrication of the clearance hinge, Miao et al [20] established a mathematical model of the deployment process of the space arm system with clearance, and studied the influence of clearance size, clearance position, clearance quantity and lubrication on the dynamics and motion stability of the space arm system. Chen et al [21, 22] established the oil film bearing capacity model of the lubricating oil clearance based on the modified Pinkus-Sternlicht model. At the same time, using the Lagrange multiplier method, they established the rigid flexible coupling dynamic model of the mechanism with lubricating clearance, and analyzed the influence of clearance value, driving speed and dynamic viscosity on the dynamic response of the mechanism.Also, they established a test device with lubrication and clearance, studied the influence of clearance value and driving speed on the mechanism considering lubrication and clearance, and verified the correctness of the theoretical model through experimental data [23, 24]. 2. Bar flexibility. Due to the large size and light materials of deployable structure after deployment, small changes in solar radiation or environmental loads will lead to structural vibration, which may cause movement stagnation of the deployable structure. Based on the floating coordinate method, Neto et al [25] studied the deployment process of the synthetic aperture radar (SAR) antenna. In order to improve the calculation efficiency, the flexible multibody equation introduced the modal component that reduces the number of balance equations. Based on the small deformation assumption and ignoring the coupling between rigid body motion and elastic member deformation, Zhang et al [26] studied the deployment dynamics and flexibility change of the simplified star grid reflector ring truss. 3. Multi scale coupling of joint and member flexibility. Large deployable structures have the characteristics of large deployment scale, many flexible components and complex configuration. The deployment process not only presents the nonlinear coupling characteristics between the large range motion of the system and the large deformation of the flexible components, but also presents the multi space-time scale coupling characteristics of the long-time scale motion of the system and the collision between the motion pairs with clearance in a very short time. Therefore, the previously mature multi rigid body system dynamics and the multi flexible body dynamics based on the floating coordinate method show some shortcomings in solving the dynamics problems of such mechanisms. Considering that large deployable structures experience large overall motion and large deformation during deployment, some scholars use ANCF method [27] to describe the deployment process of deployable structures. Luo et al [28] used the ANCF method to describe the large displacement and large deformation of variable length lanyards under the framework of Lagrangian-Euler multibody system. Peng et al [29] proposed a thermal flexible coupling dynamic analysis method for deployable structures considering the influence of temperature induced vibration caused by solar radiation flux on the deployment synchronization. At the same time, in order to obtain higher expansion accuracy, they proposed a novel coupling model of mechanical field and temperature field, and considered the two-dimensional thermal stress caused by thermal expansion. Otsuka and Makihara simulated the deployment process of space flexible aircraft wings based on the internal constraint equation of ANCF method [30]. However, the above research is mainly based on the absolute node coordinate method to analyze the dynamics of some simple multi-body mechanisms, and exposed the problems of complex dynamic model, low numerical calculation efficiency and insufficient accuracy. Therefore, the goal of this paper is to propose a comprehensive dynamic modeling and analysis method based on the absolute node coordinate method to predict accurately and efficiently the impact of the member flexibility on the dynamic performance of complex mechanism such as deployable structures.

In addition, when describing large deployable mechanisms, the ANCF method has the advantages that the mass matrix is constant, the dynamic stiffness can be automatically considered, the model accuracy is high, the rotation angle freedom is not included, and the non-incremental iteration can be used to obtain accurate solutions [31]. However, the shear deformation element based on ANCF has three locking problems: Poisson lock, thickness lock and shear lock [32 – 35]. Moreover, it has higher nonlinear elastic force and more degrees of freedom than the traditional finite element beam element [36], which leads to low calculation efficiency in the application process, limiting the application of this method in large deployable mechanism. Therefore, in order to establish the flexible multi-body dynamic model of deployable structure, this paper introduces the absolute node coordinate theory, and proposes a new non-locking planar beam element to accurately describe the large range motion and elastic deformation motion of each member of deployable structure.

This paper first introduces the classical plane shear beam element based on the absolute node coordinate method, and systematically analyzes the three locking problems and their causes. On this basis, a new non-locking plane beam element is proposed by improving the plane gradient default beam element, which can effectively avoid the locking problem in the classical beam element. Then, the kinetic energy equation and potential energy equation of the beam element are derived by using theoretical mechanics and continuum mechanics respectively. The mass matrix and stiffness matrix of the beam element are extracted by using the Lagrange equation, and the dynamic model of the beam element is established by combining the generalized force derived from the virtual work principle. Based on the beam element dynamic model, the flexible body deployment dynamic model of the whole deployable structure is established by introducing four kinds of constraint equations of the scissor line array deployable structure. In order to simplify the model, the dimension of the dynamic equation

is reduced by introducing the master-slave degree of freedom method and the proposed standard matrix method, and it is transformed from a differential algebraic equation to an ordinary differential equation. In order to eliminate the false high frequency response caused by finite element discretization, the dynamic model of the deployable structure is solved by using generalized α algorithm. Finally, the correctness and effectiveness of the method proposed in this paper are verified through the experimental test of the three element scissor deployable deployable.

2. Classical plane shear beam element

Fig. 1 is the schematic diagram of the classical plane shear beam element proposed by Shanaba, in which ϑ is the shear angle. It can be seen that the tangent line of the central axis of the beam is no longer coincident with the normal line of the beam section because the shear deformation is considered in this element.

$$\boldsymbol{S}_c=\begin{bmatrix} s_1 & 0 & ls_2 & 0 & ls_3 & 0 & s_4 & 0 & ls_5 & 0 & ls_6 & 0 \\ 0 & s_1 & 0 & ls_2 & 0 & ls_3 & 0 & s_4 & 0 & ls_5 & 0 & ls_6 \end{bmatrix}, \tag{2}$$

where:
$$\begin{aligned} s_1&=1-3\xi^2+2\xi^3 \\ s_2&=\xi-2\xi^2+\xi^3 \\ s_3&=\eta-\eta\xi \\ s_4&=3\xi^2-2\xi^3 \\ s_5&=-\xi^2+\xi^3 \\ s_6&=\eta\xi \end{aligned}$$, in which, $\xi=x/l$, $\eta=y/l$.

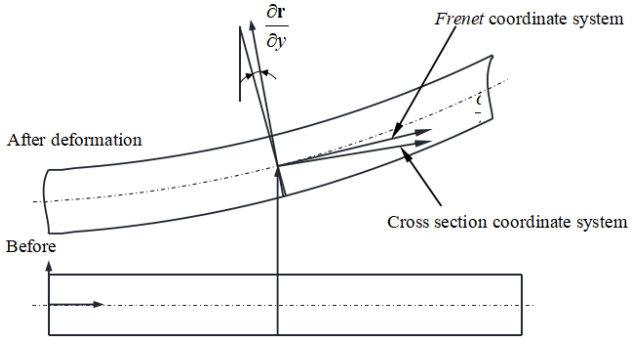

Fig. 1 Classical plane shear beam element

Although the beam element of the absolute node coordinate method can more accurately describe the large rotation and flexible body movement of the large deformation beam, the classical shear beam element will have different types of locking phenomena, among which the most significant effects are Poisson locking, shear locking and thickness locking. The three locking problems not only reduce the calculation efficiency of the classical beam element, but also have a great impact on the simulation accuracy.

2.1. Poisson locking

Fig. 2 shows a micro element on the beam element. $\sigma_x,\sigma_y,\sigma_z$ are the axial normal stress due to bending moment and the transverse normal stress along the *y* and *z* directions of the section, respectively. Therefore, the transverse normal strain using continuum mechanics can be expressed as:

According to the absolute node coordinate theory, the displacement field of the beam element under the global coordinate system is defined as [37]:

$$\boldsymbol{r}=\begin{bmatrix} r_1 \\ r_2 \end{bmatrix}=\begin{bmatrix} a_0+a_1x+a_2y+a_3xy+a_4x^2+a_5x^3 \\ b_0+b_1x+b_2y+b_3xy+b_4x^2+b_5x^3 \end{bmatrix}=\boldsymbol{S}_c\boldsymbol{e}_c, \tag{1}$$

where: $\boldsymbol{r}$ is the position vector of any point P on the beam element under the global coordinate system; a_i and b_i are the coefficients of polynomials; x is the local coordinate of the element along the axial direction ($0\le x\le l$), in which l is the length of the beam element without deformation; y is the local coordinate of the element along the transverse direction ($-h/2\le y\le h/2$, in which h is the section height of the beam element without deformation); $\boldsymbol{S}_c$ and $\boldsymbol{e}_c$ are, respectively, the shape function and generalized node coordinates of the beam element, in which the shape function of the beam element is [37]:

$$\begin{aligned} \varepsilon_y&=\frac{1}{E}\left[\sigma_y-\nu\left(\sigma_x+\sigma_z\right)\right] \\ \varepsilon_z&=\frac{1}{E}\left[\sigma_z-\nu\left(\sigma_x+\sigma_y\right)\right] \end{aligned}, \tag{3}$$

where: E is the elastic modulus and ν is the Poisson's ratio. The axial normal strain can be written as:

$$\varepsilon_x=\frac{1}{E}\left[\sigma_x-\nu\left(\sigma_y+\sigma_z\right)\right]. \tag{4}$$

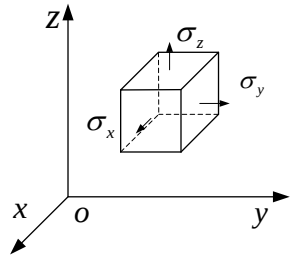

Fig. 2 Microelement on beam element

Regarding the absolute node coordinate beam element whose section can deform freely under the action of bending moment, its section should change from the initial rectangular section to trapezoidal section (as shown in Fig. 3). Then, the transverse normal stresses σ_y,σ_z on the section should be zero, that is:

$$\sigma_y=\sigma_z=0. \tag{5}$$

Substituting the above equation into Eq. (4), it can be obtained that the axial normal strain at this time is:

$$\varepsilon_x=\frac{1}{E}\sigma_x. \tag{6}$$

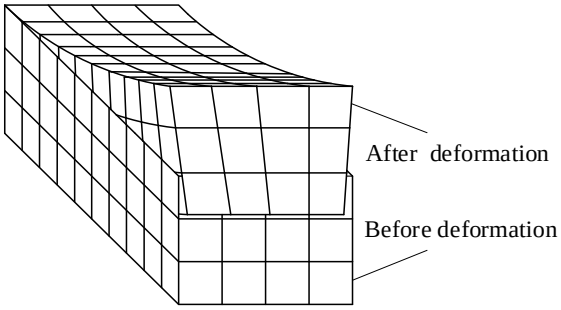

Fig. 3 Cantilever beam bending deformation

However, because the classical beam element lacks the deformation mode, it is not possible to realize the section deformation from the kinematics. Therefore, in order to ensure the balance of the finite element solution, the transverse normal strains ε_y and ε_z must be zero.

$$\varepsilon_y = \varepsilon_z = 0. \tag{7}$$

This will lead to the development of residual transverse stress, whose value can be obtained from Eq. (3).

$$\begin{aligned} \sigma_y &= \nu\left(\sigma_x + \sigma_z\right) \\ \sigma_z &= \nu\left(\sigma_x + \sigma_y\right) \end{aligned}. \tag{8}$$

Because of the occurrence of the above residual transverse stress, the axial normal strain will be affected, which is no longer shown in Eq. (6). In order to obtain its specific expression, Eq. (8) is employed to get:

$$\sigma_y + \sigma_z = \frac{2\nu}{1-\nu}\sigma_x. \tag{9}$$

By substituting Eq. (9) into Eq. (4), it is obtained:

$$\varepsilon_x = \frac{1}{E}\left(\sigma_x - \frac{2\nu^2}{1-\nu}\sigma_x\right) = \frac{\sigma_x}{E}\left(1 - \frac{2\nu^2}{1-\nu}\right). \tag{10}$$

It can be seen that when $\nu \in \left(0, 0.5\right)$, Eq. (10) and Eq. (6) are no longer identical, and the axial positive strain obtained by the former is less than the latter, so the deformation amount obtained based on the above equation will be less than the analytical solution.

2.2. Shear locking

In order to study the shear locking phenomenon of the classical plane shear beam element, the hypothesis of small deformation is first made. The axial strain ε is linearly related to the curvature and the curvature can be approximated by the second derivative of the transverse deflection, that is:

$$\varepsilon_{xx} = -yv_{xx} + u_x v_{xx}. \tag{11}$$

where: v_{xx} is the second derivative of the deflection with respect to x, and u_x is the axial deformation. Under the assumption of small deformation, the second derivative of the formula on the classical plane shear beam element can be approximated as:

$$v_{xx} = \frac{\partial^2 r_2}{\partial x^2} = 2b_4 + 6b_5 x. \tag{12}$$

It can be seen that v_{xx} is a linear function of the local coordinate x of the axial element. By substituting the above equation into Eq. (11), it is obtained:

$$\varepsilon_x = -y\left(2b_4 + 6b_5 x\right) + u_x = \varepsilon_x^b + \varepsilon_x^a, \tag{13}$$

where: ε_x^b is the axial strain related to bending deformation and ε_x^a is the axial strain related to axial deformation.

However, according to continuum mechanics, it can also be deduced that the axial strain of the classical plane beam element in the linear case is:

$$\varepsilon_x = \frac{\partial r_1}{\partial x} = a_1 + a_3 y + 2a_4 x + 3a_5 x^2. \tag{14}$$

The above formula can be classified and sorted in the same way.

$$\varepsilon_x = \varepsilon_x^a + \varepsilon_x^b, \tag{15}$$

where: $\begin{aligned} \varepsilon_x^a &= a_1 + 2a_4 x + 3a_5 x^2 \\ \varepsilon_x^b &= a_3 y \end{aligned}$.

It can be seen that the axial strain obtained by both methods is derived from two parts: one part is related to the axial deformation (ε_x^a), and the other part is related to the bending deformation (ε_x^b). It can be clearly seen from the comparison between Eq. (13) and Eq. (15) that when the continuum mechanics method is adopted, the strain ε_x^b induced by bending, based on Eq. (1), no longer changes linearly with x, but becomes a constant value along the axis direction, that is, ε_x^b changes from a first order function of x to a zero order function. The reduction of the strain ε_x^b order not only eliminates some potential deformation modes of the beam element, but also leads to false bending stiffness, which makes the classical plane shear variable beam element produce shear locking phenomenon.

2.3. Thickness locking

Compared with the traditional finite element beam element, the section of the absolute node coordinate beam element can be deformed, which leads to thickness locking.

In order to intuitively analyze the cause of the thickness locking phenomenon, the position vector of any point on the beam element is first divided into the sum of two parts, that is, the position vector of the point corresponding to the midpoint of the section and the displacement vector from the midpoint of the section to the point, as shown in Fig. 4.

The position vector can be re expressed as [32]:

$$\boldsymbol{r} = \boldsymbol{r}_c + \boldsymbol{r}_s, \tag{16}$$

where: $\boldsymbol{r}_c$ is the position vector of the point projected to the corresponding point on the centerline, and $\boldsymbol{r}_s$ is the displacement vector of the projection point to the point. Combined with Eq. (1), the specific expression of the above two vectors is [32]:

$$\boldsymbol{r}_c = s_1\boldsymbol{r}^i + ls_2\boldsymbol{r}_x^i + s_4\boldsymbol{r}^j + ls_5\boldsymbol{r}_x^j, \tag{17}$$

$$\boldsymbol{r}_s = ls_3\boldsymbol{r}_y^i + ls_6\boldsymbol{r}_y^j, \tag{18}$$

where:
$$\boldsymbol{r}^i = \begin{bmatrix} e_1 & e_2 \end{bmatrix}^T$$
$$\boldsymbol{r}^j = \begin{bmatrix} e_7 & e_8 \end{bmatrix}^T$$
$$\boldsymbol{r}_x^i = \frac{\partial \boldsymbol{r}^i}{\partial x} = \begin{bmatrix} e_3 & e_4 \end{bmatrix}^T$$
$$\boldsymbol{r}_x^j = \frac{\partial \boldsymbol{r}^j}{\partial x} = \begin{bmatrix} e_9 & e_{10} \end{bmatrix}^T .$$
$$\boldsymbol{r}_y^i = \frac{\partial \boldsymbol{r}^i}{\partial y} = \begin{bmatrix} e_5 & e_6 \end{bmatrix}^T$$
$$\boldsymbol{r}_y^j = \frac{\partial \boldsymbol{r}^j}{\partial y} = \begin{bmatrix} e_{11} & e_{12} \end{bmatrix}^T$$

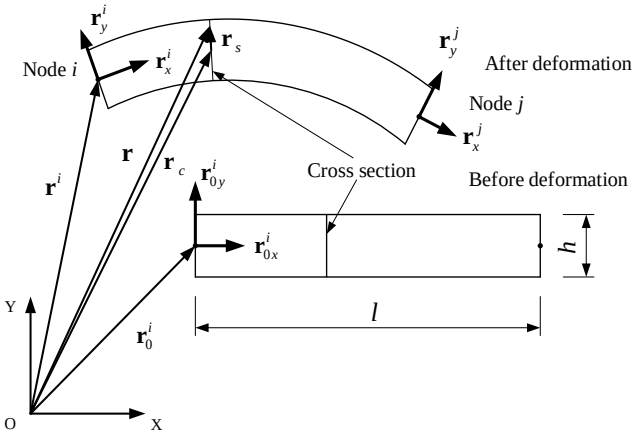

Fig. 4 Schematic diagram of classical plane beam element before and after deformation

It can be seen from Eqs. (17) and (18), since $\boldsymbol{r}_c$ is only a function of the axial coordinate x, the point on the centerline can be represented by the local coordinate x; In contrast, $\boldsymbol{r}_s$ is a linear function with respect to the axial coordinate x and the transverse coordinate y respectively, which requires the local coordinates x and y to be expressed together. By substituting Eq. (2) into Eq. (18), it is obtained:

$$\boldsymbol{r}_s = l\eta\left[(1-\xi)\boldsymbol{r}_y^i + (\xi)\boldsymbol{r}_y^j\right]. \tag{19}$$

Given that the value range of transverse coordinate y is [-h/2, h/2], the displacement vector of upper end point and lower end point of any section of classical beam element can be obtained by substituting it into Eq. (19).

$$\begin{aligned} \boldsymbol{r}_s^t &= \boldsymbol{r}_s(x, h/2) = \frac{h}{2}\left[(1-\xi)\boldsymbol{r}_y^i + (\xi)\boldsymbol{r}_y^j\right] \\ \boldsymbol{r}_s^b &= \boldsymbol{r}_s(x, -h/2) = -\frac{h}{2}\left[(1-\xi)\boldsymbol{r}_y^i + (\xi)\boldsymbol{r}_y^j\right] \end{aligned}. \tag{19}$$

By subtracting the above two equations:

$$\Delta\boldsymbol{r}_s = \boldsymbol{r}_s^t - \boldsymbol{r}_s^b = h\left[(1-\xi)\boldsymbol{r}_y^i + (\xi)\boldsymbol{r}_y^j\right]. \tag{20}$$

Obviously, the modulus of the above vector is the thickness of the section. To facilitate the analysis, the following assumptions are made:

$$\boldsymbol{r}_s^v = (1-\xi)\boldsymbol{r}_y^i + (\xi)\boldsymbol{r}_y^j. \tag{21}$$

As $\boldsymbol{r}_s^v$ is the linear interpolation of the slope coordinate vectors $\boldsymbol{r}_y^i$ and $\boldsymbol{r}_y^j$, when the head and tail sections of the beam element are no longer parallel, as shown in Fig. 5, the modulus of $\boldsymbol{r}_s^v$ will be less than 1, and the modulus of the vector $\Delta\boldsymbol{r}_s$ will be less than the initial value h, that is, the thickness of any section will be less than h. Therefore, when the beam element is deformed, its theoretical deformation configuration is shown in Fig. 6.

It can be seen from the Fig. 6 that, as a result of linear interpolation of rotation vectors $\boldsymbol{r}_y^i$ and $\boldsymbol{r}_y^j$, the section of the beam element shrinks gradually from both sides to the middle and shrinks more as it gets closer to the middle. It is worth noting that this phenomenon will become more and more significant as the angle between the two slope vectors $\boldsymbol{r}_y^i$ and $\boldsymbol{r}_y^j$ increases. Especially when the two vectors $\boldsymbol{r}_y^i$ and $\boldsymbol{r}_y^j$ are collinear and opposite, the linear interpolation of the transverse slope coordinates will lead to a very serious false deformation mode. It can be seen from Eq. (21) that there must be a zero vector in the middle of the beam element, that is, the section thickness at this location is zero, which is completely inconsistent with the actual situation.

From the above discussion, we can see that the only way to prevent the middle section of a classical beam element from shrinking during bending is to keep the sections at both ends of the beam element always parallel, as shown in Fig. 7. However, this will lead to excessive shear deformation.

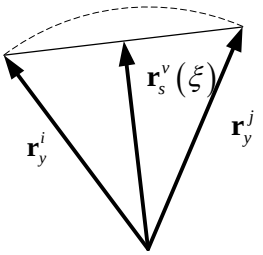

Fig. 5 Linear interpolation of section slope vector

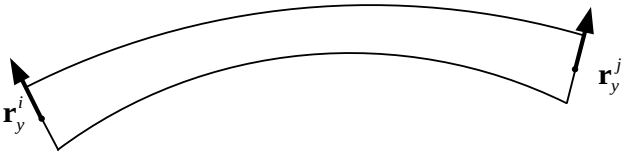

Fig. 6 Deformation configuration of classical plane beam element

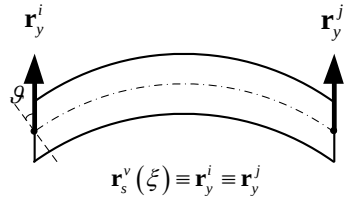

Fig. 7 Deformation configuration when two end faces are parallel

3. A novel non-locking plane beam element

In order to eliminate the locking problem of the classical shear beam element, a new non-locking planar beam element is proposed in this paper. The beam element is characterized by the position coordinates of three nodes, the transverse slope vector $\partial \boldsymbol{r}/\partial y$ and the tangential slope vector $\partial \boldsymbol{r}/\partial x$ at the middle node, as shown in Fig. 8.

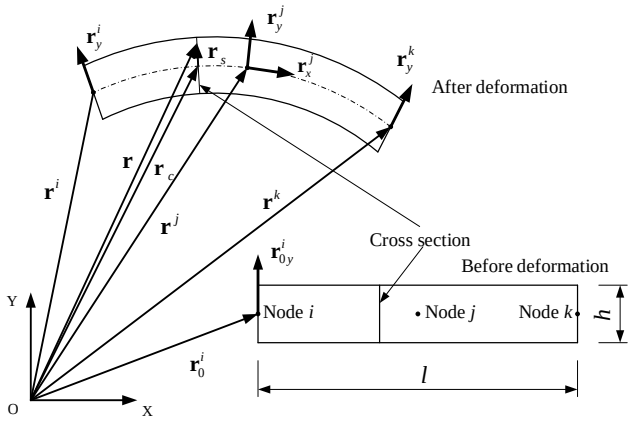

Fig. 8 Planar beam element without locking

The absolute node coordinates of the non-locking plane beam element can be expressed as:

$$\boldsymbol{e}_n = \begin{bmatrix} \boldsymbol{e}^i & \boldsymbol{e}^j & \boldsymbol{e}^k \end{bmatrix}^T = \begin{bmatrix} \boldsymbol{r}^i & \boldsymbol{r}_y^i & \boldsymbol{r}^j & \boldsymbol{r}_x^j & \boldsymbol{r}_y^j & \boldsymbol{r}^k & \boldsymbol{r}_y^k \end{bmatrix}^T, \tag{22}$$

where: $\boldsymbol{r}^i, \boldsymbol{r}^j, \boldsymbol{r}^k$ are the global position vectors of nodes *i*, *j* and *k* respectively, that is:

$\boldsymbol{r}^i = \boldsymbol{r}\big|_{x=0,\,y=0}$ $\boldsymbol{r}^j = \boldsymbol{r}\big|_{x=l/2,\,y=0}$ $\boldsymbol{r}^k = \boldsymbol{r}\big|_{x=l,\,y=0}$.

Noted, $\boldsymbol{r}_y^i, \boldsymbol{r}_y^j, \boldsymbol{r}_y^k$ are the section slope at the corresponding node.

$$\boldsymbol{r}_y^i = \frac{\partial \boldsymbol{r}^i}{\partial y}\bigg|_{x=0,\,y=0} \quad \boldsymbol{r}_y^j = \frac{\partial \boldsymbol{r}^j}{\partial y}\bigg|_{x=l/2,\,y=0} \quad \boldsymbol{r}_y^k = \frac{\partial \boldsymbol{r}^k}{\partial y}\bigg|_{x=l,\,y=0}.$$

$\boldsymbol{r}_x^j$ is the tangent slope at the node.

$$\mathbf{r}_x^j = \frac{\partial \mathbf{r}^j}{\partial x}\bigg|_{x=l/2,\,y=0}.$$

Accordingly, the upper displacement field of non-locking planar beam element can be defined as:

$$\boldsymbol{r} = \begin{bmatrix} r_1 \\ r_2 \end{bmatrix} = \begin{bmatrix} a_0 + a_1 x + a_2 y + a_3 xy + a_4 x^2 + a_5 x^2 y + a_6 x^3 \\ b_0 + b_1 x + b_2 y + b_3 xy + b_4 x^2 + b_5 x^2 y + b_6 x^3 \end{bmatrix} = \boldsymbol{S}_n \boldsymbol{e}_n. \tag{23}$$

Thus, the shape function of the plane beam element without locking can be obtained as:

$$\boldsymbol{S}_n = \begin{bmatrix} s_1\boldsymbol{I} & s_2\boldsymbol{I} & s_3\boldsymbol{I} & s_4\boldsymbol{I} & s_5\boldsymbol{I} & s_6\boldsymbol{I} & s_7\boldsymbol{I} \end{bmatrix}, \tag{24}$$

where: $\boldsymbol{I}$ is the unit matrix, and the shape function items are as follows:

$$\begin{aligned} s_1 &= 1 - 5\xi + 8\xi^2 - 4\xi^3 \\ s_2 &= l\eta\left(1 - 3\xi + 2\xi^2\right) \\ s_3 &= 4\xi - 4\xi^2 \\ s_4 &= l\xi\left(-2 + 6\xi - 4\xi^2\right) \\ s_5 &= l\eta\left(4\xi - 4\xi^2\right) \\ s_6 &= \xi - 4\xi^2 + 4\xi^3 \\ s_7 &= l\eta\left(-\xi + 2\xi^2\right) \end{aligned}$$

It can be seen from the above equation that compared with the classical plane shear beam element, the shape function of the non-locking plane beam element has an additional $\eta\xi^2$ term, which will improve the performance of the beam element. It is worth noting that in order to avoid Poisson locking, this paper adopts the method of making Poisson's ratio 0.

4. Beam element dynamic model

According to theoretical mechanics, the kinetic energy of the beam element is:

$$T_e = \frac{1}{2}\int_V \rho \dot{\boldsymbol{e}}^T \boldsymbol{S}^T \boldsymbol{S} \dot{\boldsymbol{e}} dV = \frac{1}{2}\dot{\boldsymbol{e}}^T \boldsymbol{M}_e \dot{\boldsymbol{e}}, \tag{25}$$

where: $\dot{\boldsymbol{e}}$ is the absolute node velocity; $\boldsymbol{M}_e$ is the mass matrix of beam element; $\boldsymbol{M}_e = \int_V \rho \boldsymbol{S}^T \boldsymbol{S} dV$.

According to continuum mechanics, the Green Lagrangian strain tensor is:

$$\boldsymbol{\varepsilon}_L = \frac{1}{2}\begin{bmatrix} \boldsymbol{e}^T \boldsymbol{S}_a \boldsymbol{e} - 1 & \boldsymbol{e}^T \boldsymbol{S}_c \boldsymbol{e} \\ \boldsymbol{e}^T \boldsymbol{S}_c \boldsymbol{e} & \boldsymbol{e}^T \boldsymbol{S}_b \boldsymbol{e} - 1 \end{bmatrix}, \tag{26}$$

in which:

$$\begin{aligned} \boldsymbol{S}_a &= \sum_{i=1}^{2} \boldsymbol{S}_{ix}^T \boldsymbol{S}_{ix} \cos^2\theta - \boldsymbol{S}_{ix}^T \boldsymbol{S}_{iy} \sin\theta\cos\theta - \boldsymbol{S}_{iy}^T \boldsymbol{S}_{ix} \sin\theta\cos\theta + \boldsymbol{S}_{iy}^T \boldsymbol{S}_{iy} \sin^2\theta \\ \boldsymbol{S}_b &= \sum_{i=1}^{2} \boldsymbol{S}_{ix}^T \boldsymbol{S}_{ix} \cos^2\theta + \boldsymbol{S}_{ix}^T \boldsymbol{S}_{iy} \sin\theta\cos\theta - \boldsymbol{S}_{iy}^T \boldsymbol{S}_{ix} \sin\theta\cos\theta + \boldsymbol{S}_{iy}^T \boldsymbol{S}_{iy} \sin^2\theta, \\ \boldsymbol{S}_c &= \sum_{i=1}^{2} \boldsymbol{S}_{ix}^T \boldsymbol{S}_{ix} \sin\theta\cos\theta + \boldsymbol{S}_{ix}^T \boldsymbol{S}_{iy} \cos^2\theta - \boldsymbol{S}_{iy}^T \boldsymbol{S}_{ix} \sin^2\theta - \boldsymbol{S}_{iy}^T \boldsymbol{S}_{iy} \sin\theta\cos\theta \end{aligned}$$

where: $\boldsymbol{S}_{ix}$ and $\boldsymbol{S}_{iy}$ are the partial derivatives of the shape function matrix $\boldsymbol{S}$ with respect to x and y in the ith row, i=1,2. Based on the generalized Hooke's law, the constitutive equation is:

$$\boldsymbol{\sigma} = \boldsymbol{E}\boldsymbol{\varepsilon}, \tag{27}$$

where: σ is the second Piola Kirchhoff stress vector. Therefore, the elastic potential energy expression of the beam element can be written as:

$$U_e = \frac{1}{2}\int_V \boldsymbol{\sigma}^T \boldsymbol{\varepsilon} dV. \tag{28}$$

The elastic force equation of the beam element can be obtained by solving the partial derivative of the generalized coordinate e of the equation, which is:

$$\boldsymbol{Q}_e^e = -\frac{\partial U_e}{\partial \boldsymbol{e}} = -\boldsymbol{K}_e \boldsymbol{e}, \tag{29}$$

where: $\boldsymbol{K}_e$ is the stiffness matrix of the beam element.

$$\boldsymbol{K}_e = (\lambda + 2\mu)\boldsymbol{K}_1 + \lambda \boldsymbol{K}_2 + \mu \boldsymbol{K}_3, \tag{30}$$

$$\boldsymbol{K}_1 = \frac{1}{4}\int_V \left[\boldsymbol{S}_a^*\left(\boldsymbol{e}^T\boldsymbol{S}_a\boldsymbol{e}-1\right) + \boldsymbol{S}_b^*\left(\boldsymbol{e}^T\boldsymbol{S}_b\boldsymbol{e}-1\right)\right]dV$$

$$\boldsymbol{K}_2 = \frac{1}{4}\int_V \left[\boldsymbol{S}_b^*\left(\boldsymbol{e}^T\boldsymbol{S}_a\boldsymbol{e}-1\right) + \boldsymbol{S}_a^*\left(\boldsymbol{e}^T\boldsymbol{S}_b\boldsymbol{e}-1\right)\right]dV$$

in which: $\boldsymbol{K}_3 = \int_V \left[\boldsymbol{S}_c^*\left(\boldsymbol{e}^T\boldsymbol{S}_c\boldsymbol{e}\right)\right]dV$.

$$\boldsymbol{S}_a^* = \boldsymbol{S}_a^T + \boldsymbol{S}_a$$

$$\boldsymbol{S}_b^* = \boldsymbol{S}_b^T + \boldsymbol{S}_b$$

$$\boldsymbol{S}_c^* = \boldsymbol{S}_c^T + \boldsymbol{S}_c$$

After obtaining the kinetic energy equation and elastic force, the dynamic equation of the beam element can be obtained using the second type of Lagrange equation, which can be defined as:

$$\frac{\mathrm{d}}{\mathrm{d}t}\frac{\partial T_e}{\partial \dot{\boldsymbol{e}}} = \boldsymbol{Q}_e + \boldsymbol{Q}_e^e. \tag{31}$$

By substituting Eqs. (26) and (29) into the above equation:

$$\boldsymbol{M}_e\ddot{\boldsymbol{e}} + \boldsymbol{K}_e\boldsymbol{e} = \boldsymbol{Q}_e. \tag{32}$$

The above equation is the dynamic equation of the beam element, where $\ddot{\boldsymbol{e}}$ is the absolute node acceleration vector, and $\boldsymbol{Q}_e$ is the generalized force.

5. Dynamic model of linear array deployable structure based on scissor-like element

The scissor deployable structure is composed of scissor-like elements, which is the smallest element of the deployable structure. As shown in Fig. 9, it is composed of bar ab, bar cd and hinges at points e and e′. At both ends of each bar, namely points a, b, c and d, there is a hinge hole for connecting with the support or other type deployable mechanisms. In this paper, the deployable structure of Fig. 10 composed of scissor elements arrayed along a line will be studied.

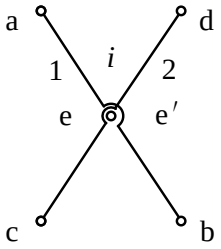

Fig. 9 Scissor-like element

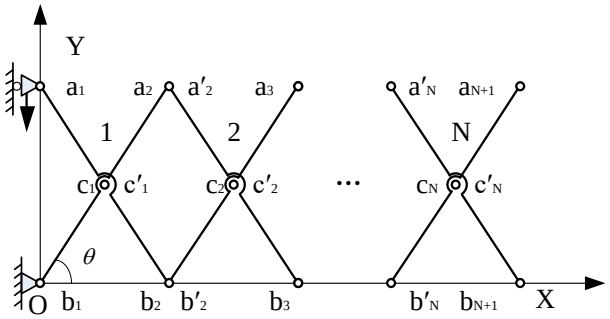

Fig. 10 Scissor linear array deployable structure

According to the configuration characteristics of scissor deployable structure, this paper proposes a standard matrix method to adjust the position coordinates within the element and between adjacent elements, as well as the arrangement order of gradient vectors, in order to reassemble the stiffness matrix and mass matrix, eliminate the constraint equations between flexible bodies, and reduce the difficulty of solving the problem.

The node coordinates of the scissor element can be expressed as:

$$\boldsymbol{q}_s = \left[\boldsymbol{r}_a \quad \boldsymbol{r}_{a,y} \quad \boldsymbol{r}_e \quad \boldsymbol{r}_{e,x} \quad \boldsymbol{r}_{e,y} \quad \boldsymbol{r}_b \quad \boldsymbol{r}_{b,y} \quad \boldsymbol{r}_c \quad \boldsymbol{r}_{c,y} \quad \boldsymbol{r}_{e'} \quad \boldsymbol{r}_{e',x} \quad \boldsymbol{r}_{e',y} \quad \boldsymbol{r}_d \quad \boldsymbol{r}_{d,y}\right]. \tag{33}$$

Using the transformation matrix $\boldsymbol{T}_1$, the coordinate order of $\boldsymbol{q}_s$ can be adjusted as follows:

$$\begin{aligned} &\boldsymbol{q}_{s1} = \left[\boldsymbol{r}_a \quad \boldsymbol{r}_{a,y} \quad \boldsymbol{r}_b \quad \boldsymbol{r}_{b,y} \quad \boldsymbol{r}_e \quad \boldsymbol{r}_{e,x} \quad \boldsymbol{r}_{e,y} \quad \boldsymbol{r}_{e'} \quad \boldsymbol{r}_{e',x} \quad \boldsymbol{r}_{e',y} \quad \boldsymbol{r}_c \quad \boldsymbol{r}_{c,y} \quad \boldsymbol{r}_d \quad \boldsymbol{r}_{d,y}\right], \\ &\boldsymbol{q}_{s1} = \boldsymbol{T}_1\boldsymbol{q}_s \end{aligned} \tag{34}$$

where: $\boldsymbol{T}_1$ is the transformation matrix, which can be obtained by filtering. Supposing that it is a full n×n matrix, the elements in the matrix are determined by the following constraints.

$$\begin{cases} \boldsymbol{T}_{1ij}\cdot\boldsymbol{q}_{s1} = \boldsymbol{q}_s \Rightarrow \boldsymbol{T}_{1ij} = 1 \\ \boldsymbol{T}_{1ij}\cdot\boldsymbol{q}_{s1} \neq \boldsymbol{q}_s \Rightarrow \boldsymbol{T}_{1ij} = 0 \end{cases}, \tag{35}$$

where: $i, j = 1,2 \cdots n$. It is noted that i is in the external loop layer during programming calculation.

$$\boldsymbol{q}_{s'} = \boldsymbol{T}_2 \boldsymbol{q}_{s1} = \begin{bmatrix} \boldsymbol{r}_a & \boldsymbol{r}_c & \boldsymbol{r}_{a,y} & \boldsymbol{r}_{c,y} & \boldsymbol{r}_e & \boldsymbol{r}_{e,x} & \boldsymbol{r}_{e,y} & \boldsymbol{r}_{e',x} & \boldsymbol{r}_{e',y} & \boldsymbol{r}_{d,y} & \boldsymbol{r}_{b,y} & \boldsymbol{r}_d & \boldsymbol{r}_b \end{bmatrix}, \tag{36}$$

where: $\boldsymbol{T}_2$ is the transformation matrix, which can be obtained by the same method as in Formula (35). The modified node coordinates of the first scissor element can be obtained through calculation, and its matrix dimension is reduced from 28×28 to 26×26, which indicates that the computational complexity of the motion equation will be reduced. Similarly, the mass matrix and stiffness matrix of the first element can be obtained. The mass matrix is a constant matrix, which can be obtained according to the same conversion process as above. The stiffness matrix can be obtained by substituting the initial parameters into Formula (29) and converting the corresponding coordinate sequence based on the absolute node coordinate method. After obtaining the relevant information of the first element, the total stiffness matrix and mass matrix of the linear array deployable structure can be obtained by (*n*-1) addition of the corresponding matrix.

Then, considering the boundary constraints, the dynamic equation of the scissor deployable structure can be established using the first kind of Lagrangian equation.

$$\begin{cases} \boldsymbol{M}^d \ddot{\boldsymbol{q}}^d + \boldsymbol{K}^d \boldsymbol{q}^d + \boldsymbol{\Phi}_{\boldsymbol{q}}^d \boldsymbol{\lambda}_d = \boldsymbol{Q}^d \\ \boldsymbol{\Phi}^d \left(\boldsymbol{q}^d, t \right) = \boldsymbol{0} \end{cases}, \tag{37}$$

where: $\boldsymbol{q}^d$ and $\boldsymbol{\Phi}^d \left(\boldsymbol{q}^d, t \right)$ are, respectively, the node coordinate vector and constraint equation of the scissor deployable structure after adjustment,; $\boldsymbol{\Phi}_{\boldsymbol{q}}^d$ is the derivative of the constraint equation to the node coordinate *qd*, and $\boldsymbol{\lambda}_d$ is the Lagrangian factor of the scissor element deployable structure.

In terms of solving dynamic equations, considering the configuration characteristics and assembly methods of the scissor deployable structure, in order to dissipate the high frequency response while maintaining the low frequency response of the system, the simplified generalized α method is selected to solve the nonlinear dynamic problems of scissor deployable structures. Please refer to literature [29] for the specific solution process.

6. Validation of the novel non-locking beam element

6.1. Verification of shear locking and thickness locking from statics

Taking a cantilever beam and a simply supported beam as examples, shown in Fig. 11, the effects of shear locking and thickness locking are analyzed respectively to verify the correctness of the beam element proposed in this paper. The cantilever beam shown in Fig. 13 is analyzed for stress and deformation. The left end of the cantilever beam is fixed, and bending deformation occurs only under the external force *F* at the right end.

According to material mechanics, the deflection of the cantilever beam derived from Euler beam theory can be expressed as:

In order to eliminate the hinge constraint inside the element and facilitate the array assembly, the node coordinate $\boldsymbol{q}_{s1}$ of the scissor element can be further rewritten as:

$$\delta^{analytical} = \frac{Fx^3}{3EI}. \tag{38}$$

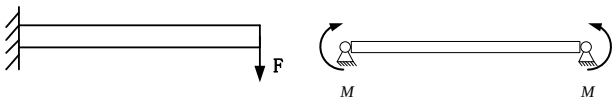

Fig. 11 Loading of cantilever beam and simply supported beam

The classical plane shear beam element and the beam element proposed in this paper are also used to derive the deflection of the cantilever beam, as follows:

$$\delta_{max}^c = \frac{Fx\left(27x^2 + 16h^2\right)}{108EI}, \tag{39}$$

$$\delta_{max}^n = \frac{2Fx\left(2x^2 + h^2\right)}{12EI}, \tag{40}$$

where the superscript *analytical*; *c*, and *n* respectively represent the material mechanics theory, classical beam element, and the proposed beam element; *I* is the moment of inertia of the beam section. The geometric and material parameters of the cantilever beam are shown in Table 1. The maximum deflection results and beam deformation obtained from the three methods are shown in Table 2 and Fig. 12 respectively.

Table 1

Dimensions and material parameters of cantilever beam

Parameter	Value
Bar length *L*	1m
Section height *h*	0.02 m
Section width *c*	0.02 m
Elastic modulus *E*	2×10^8 Pa
Poisson's ratio ν	0
Density ρ	7750 kg/m^3

Table 2

Beam deformation

Category	Numerical	Error
Analytic solution	0.124999998 m	-
Classical plane shear beam element	0.093771050 m	25 %
Beam element proposed in this paper	0.125023472 m	0.02 %

It can be seen from Table 2 and Fig. 12 that there are obvious differences between the classical plane shear beam element and the analytical solution. Because Poisson's locking has been avoided by taking Poisson's ratio equal to 0, and the thickness locking is only obvious in large bending, especially when the two ends are parallel and opposite, the difference is mainly caused by the shear locking. By comparison, we can find that the calculation results of the beam element proposed in this paper are basically consistent with the analytical solution, which shows that the proposed element effectively avoids the shear locking problem.

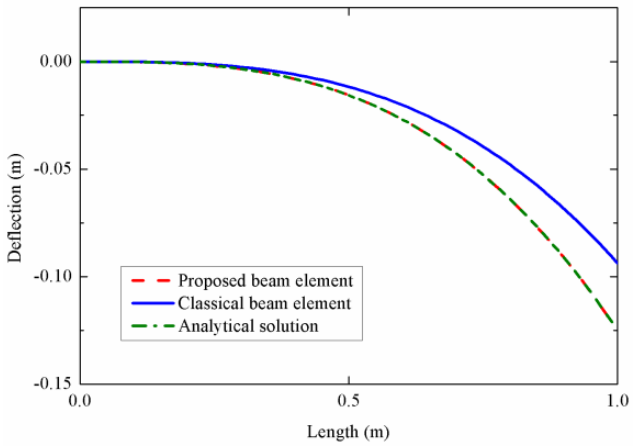

Fig. 12 Deformation of cantilever beam

In order to verify the thickness locking, the classical beam element and the proposed beam element are used to analyze the stress and deformation of the simply supported beam shown in Fig. 11, where the beam is only affected by the bending moment *M*, and the two bending moment directions are respectively clockwise and counterclockwise.

According to the theory of material mechanics, the thickness of a simply supported beam can be regarded as constant during the deformation process, that is:

$$\Delta \mathbf{r}^{analytical} = h. \tag{41}$$

Using the classical beam element and the proposed beam element, the thickness of the middle section of the element can be expressed as:

$$\Delta \mathbf{r}^{c} = h\sqrt{1-\left[\frac{ML}{2EI}\right]^2}, \tag{42}$$

$$\Delta \mathbf{r}^{n} = h. \tag{43}$$

From the above formulas, it can be clearly observed that the section thickness of the classical plane shear beam element is related to the magnitude of the bending moment it bears, and must be less than *h*. However, the section thickness of the proposed beam element is independent of the bending moment and is identical to *h*. The geometric and material parameters of the simply supported beam (as shown in Table 1) are substituted into the above formulas, and the calculation results are shown in Table 3. It can be seen from the table that the section thickness of the proposed beam element is consistent with the theoretical value, both of which have initial values of 0.02 m, while the section thickness of the classical plane shear beam element has shrunk to a certain extent, becoming 0.0185 m, indicating that the thickness locking phenomenon occurred in the classical beam element after the large bending deformation of the simply supported beam. Through the comparison between the three, it is fully verified that the proposed beam element effectively avoids the thickness locking problem.

The above two examples prove that the calculation results of the proposed beam element are closer to the analytical solution than the classical plane shear beam element, which fully demonstrates the correctness of the method in avoiding shear lock and thickness lock.

Table 3

Thickness of beam middle section

Category	Numerical	Error
Analytic solution	0.02 m	-
Classical plane shear beam element	0.0185 m	7.5 %
Beam element proposed in this paper	0.02 m	0 %

6.2. Validation of shear locking and thickness locking from dynamics

In the dynamics part, the correctness of the beam element proposed in this paper is verified by comparing with the results of ANSYS analysis. In order to reduce the amount of calculation, a flexible simple pendulum is used as a case, in which the flexible beam is connected with the support through hinge and suspended in the air, and can rotate and deform freely under the gravity, as shown in Fig. 13. In addition, the gravity acceleration g is taken as 9.81 m/s^2.

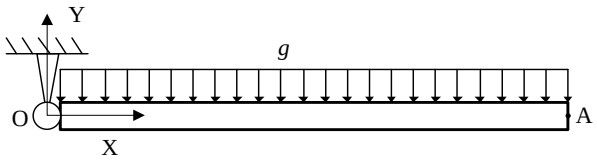

Fig. 13 Flexible simple pendulum

The dimension parameters and material parameters of the beam are shown in Table 1. ANSYS solid element (Transient Structural), classical beam element and the proposed improved beam element are used to establish their motion models and conduct the dynamic analysis. The analysis and simulation results are shown in Figs. 14 and 15.

Fig. 14 shows the displacement of point A along the X axis calculated by three beam elements, and Fig. 15 shows the deformation of the simple pendulum at different time.

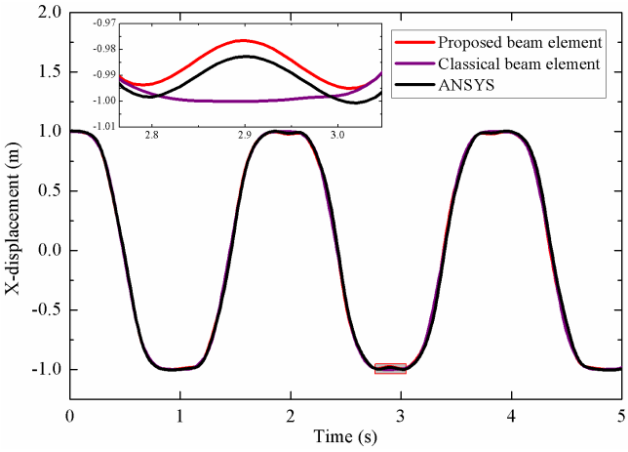

Fig. 14 Displacement of point A along X-axis calculated by the three types of beam elements

It can be seen from the figures that the beam element proposed in this paper is in good agreement with the ANSYS results, which verifies that the proposed beam element solves the three locking problems, and can explain the motion and deformation of the beam from the perspective of dynamics. In Fig. 14, by comparing with the analysis results of the classical plane shear beam element, it can be found

that the classical beam element has almost no elastic deformation at the position with the maximum swing amplitude, which shows that the classical beam element has greater "stiffness" than the other two beam elements, and proves that the locking problem of the classical beam element will affect the accuracy of its simulation. At the same time, it is proved again that the beam element proposed in this paper avoids the locking problem of the classical beam element.

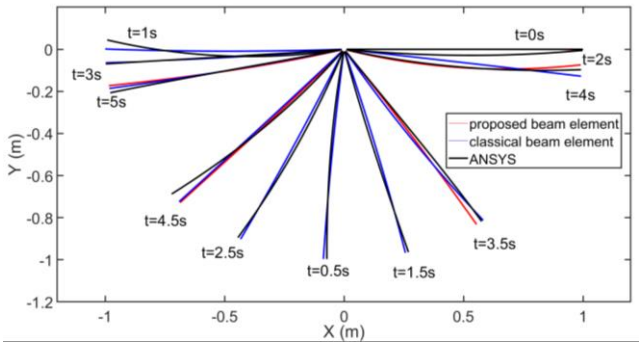

Fig. 15 Deformation of simple pendulum at different time

7. Simulation and experiment

7.1. Classical example simulation

The deployable structure composed of 3 scissor-like elements (Fig. 16) is employed to analyze its dynamics, where θ is the deployaing angle. The origin of the inertial coordinate system O is fixed at point b_1. Constraints are applied at points a_1 and b_1, respectively, limiting the translation of point a_1 along the X axis and point b_1 along the X axis and Y axis. The driving force F along the negative Y axis is applied at point a_1. The bars of the scissor deployable structure are hollow beams (thin-walled tubes). The bar length L is 1 m, the cross section is a square, 10 mm×10 mm, the wall thickness is 0.4 mm, and the driving force F is -0.1 N. The initial deploying angle θ is 80°. Specific material parameters are listed in Table 4.

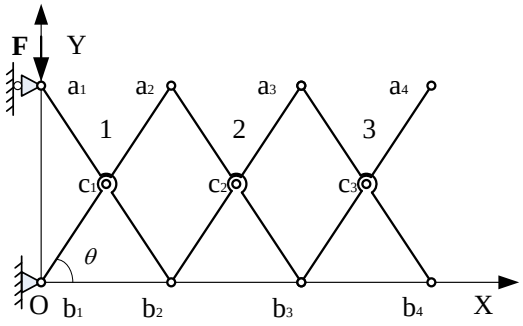

Fig. 16 Scissor linear array deployable structure composed of 3 elements

Table 4

Material parameters of scissor linear array deployable structure

Parameter	Value
Elastic modulus E	152 GPa
Poisson's ratio v	0.3
Density ρ	8026 kg/m^3

The proposed modeling method and numerical solution method are used to analyze the dynamics of the scissor linear array deployable structure, and the results are compared with the multi rigid body dynamics, shown in Fig. 17. The two curves in the figure respectively represent the dynamic characteristic change process of point a_4 on the deployable structure considering the flexibility and rigidity of the member. It can be found that the deployment process of deployable structure driven by constant force is a variable acceleration movement. In the first and second stages of the deployment process, the changes of displacement, velocity and acceleration are relatively gentle; At the later stage of deployment, especially after 10 seconds, the displacement, velocity and acceleration will change rapidly, and the absolute value of the latter two will also increase rapidly. Therefore, the sudden locking at the end of the constant force drive will have a great impact on the stability of the deployable structure. It is necessary to systematically analyze the dynamic behavior under this drive.

Observe Fig. 17 and find that the dynamic behavior of deployable structure is significantly different after considering the flexibility and rigidity of components. Displacement, velocity and acceleration have experienced different degrees of vibration (the acceleration vibration is the most significant), which will lead to the instability of deployable structure's deployment motion, and may also cause resonance and syntony of spacecraft. In addition, due to the elastic deformation with tensile, shear and bending components, there are also some differences between the expansion displacement of the flexible body and the rigid body of the deployable structure. The maximum displacement along the X axis and the Y axis are 0.0065 m and 0.0059 m respectively.

The numerical simulation results of the deployment motion of each point on the same horizontal line of the flexible deployable structure are shown in Fig. 18. From the displacement curves (a) and (b), the flexibility of the member mainly affects the synchronization of the movement of the points on the same horizontal line of the deployable structure (the movement of the points on the same horizontal line is consistent or proportional), which is particularly evident in Fig. 18, b. The displacement curves of points a_2, a_3 and a_4 along the Y axis are no longer completely coincident, and the displacement of the three points along the Y axis gradually varies with the expansion movement. The displacement difference between the three points reached the maximum at 11.39 s, and the maximum difference was (0.00274+0.00230) = 0.00504 m.

From the velocity curves (c) and (d) and the acceleration curves (e) and (f) of points a_2, a_3 and a_4 in Fig. 18, it can be clearly observed that the velocities and accelerations of the three points are not synchronized along the Y axis, but also have obvious vibration, and the corresponding vibration of point a_4 is always the largest and most obvious. On the other hand, it can be seen that the velocities of points a_2, a_3 and a_4 along the X axis reach their peak values in 10.8 s to 10.9 s, and then decrease rapidly. The reason for this phenomenon is that the direction of the corresponding acceleration turns from positive to negative and the absolute value increases rapidly.

7.2. Experimental verification

The flexible body dynamics experiment platform of three scissor element line array deployable structure was built to verify the numerical finding of this paper. The experimental setup is shown in Fig. 19, which mainly consists

of drive module, control module and measurement module according to their functions. 1. Drive module. The drive module is composed of a motor, a ball screw module and a sliding block. The motor is connected with the screw through a coupling to make the screw rotate so as to transmit power to the sliding block; 2. Control module. The control module is composed of a computer, a controller, a driver and a DC power supply, and the latter three are integrated in the drive control box; 3. Measuring module. including pull wire displacement sensor and RS485 signal converter. The pull head of the displacement sensor is fixed at the end point of the scissor deployable structure. The RS485 signal converter converts the displacement signal collected by the displacement sensor into a USB signal that can be recognized by the computer, and then uses the serial port debugging software to receive and record the data.

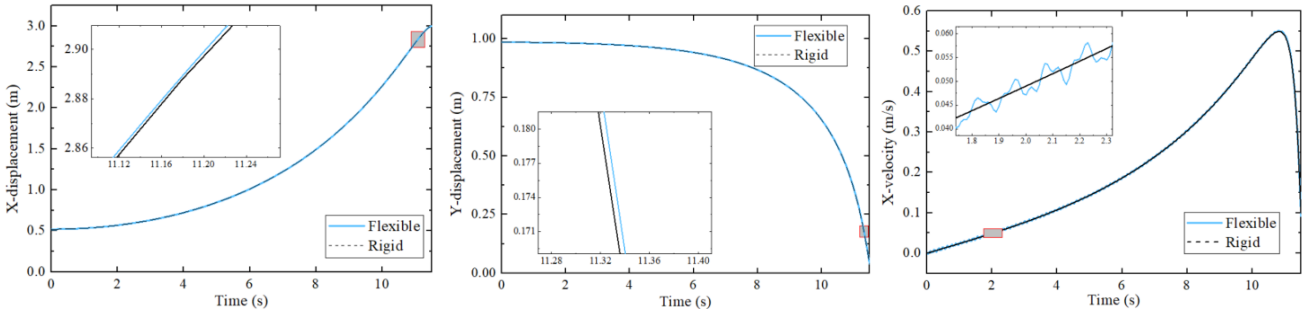

a) Displacement along X axis b) Displacement along Y axis c) Velocity along X axis

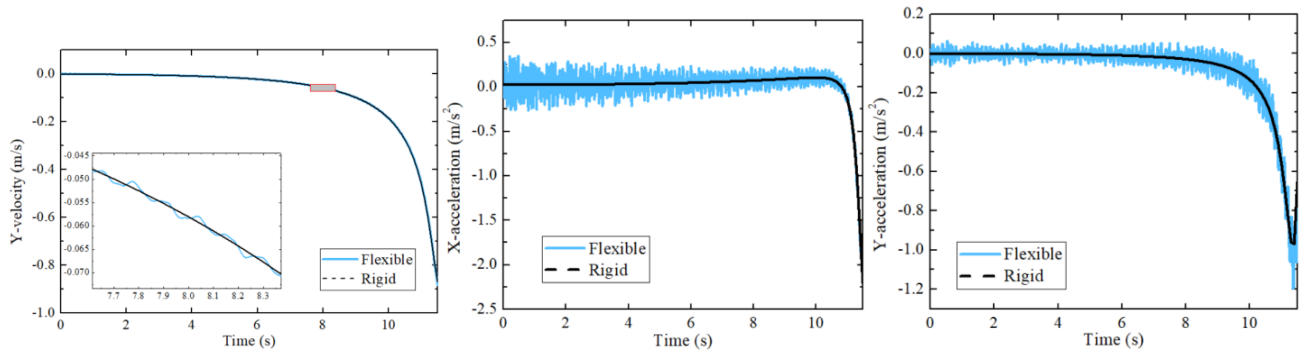

d) Velocity along Y axis e) Acceleration along X axis f) Acceleration along Y axis

Fig. 17 Comparison between flexible body dynamics and rigid body dynamics of scissor deployable structure

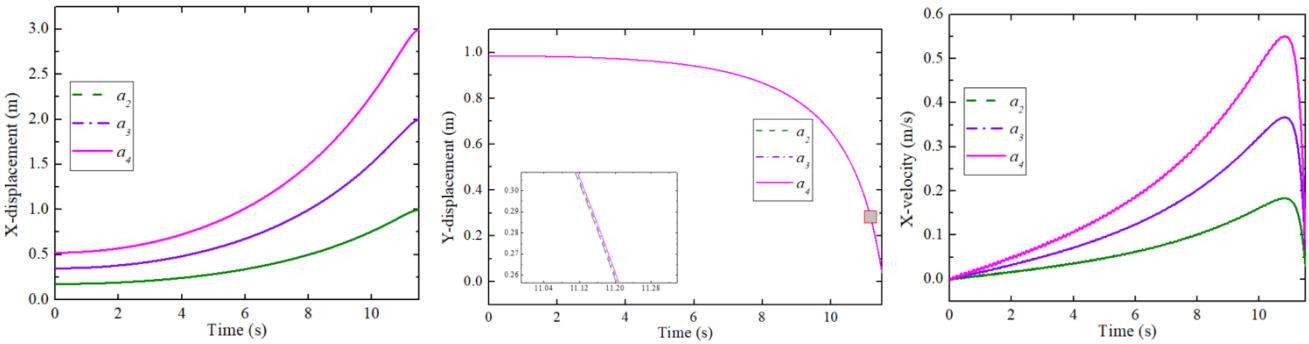

a) Displacement along X axis b) Displacement along Y axis c) Velocity along X axis

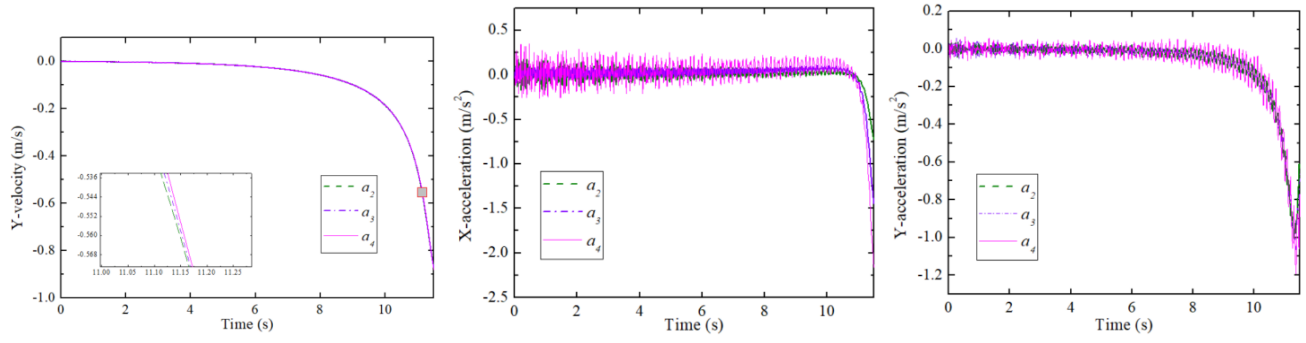

d) Velocity along Y axis e) Acceleration along X axis f) Acceleration along Y axis

Fig. 18 Deployment motion of points a_2, a_3 and a_4 on the deployable structure

In order to verify the correctness of the flexible body dynamics model of the scissor deployable structure established in this paper, the theoretical and experimental results of the deployable structure composed of three scissor elements (bar length 0.5 m) are compared and analyzed. It should be noted that the scissor deployable structure is a planar mechanism, so the planar element is used for analysis.

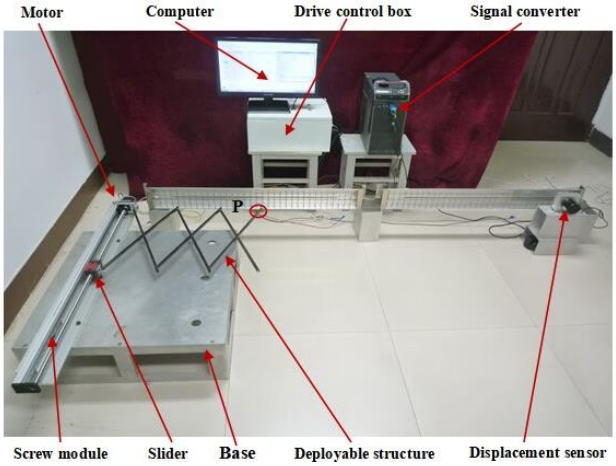

Fig. 19 Scissor linear array deployable structure experimental platform

When the deployment time is 50 s and the bar length is 0.5 m, the displacement simulation results and experimental results of the measured point *P* along the X-axis are shown in Fig. 20.

It can be seen from Fig. 20 that the simulated displacement curve of the deployable structure's deployment motion is basically consistent with the experimental displacement curve, and both experence rapid increase first, then gradual increase. In addition, the difference between the two displacement curves mainly occurs at the beginning and end of the deployment, and the maximum error occurs at the end of the deployment, which is 0.0502 m. Correspondingly, the maximum error rate is 3.6%, which is within the engineering error range. It is speculated that the reason for the difference in the initial stage of deployment may be that the structure will undergo slight elastic deformation in order to balance the friction force at the hinge, which will cause the experimental measured displacement to lag behind the theoretical simulated displacement. On the other hand, there are two main reasons for the obvious differences at the end of deployment. One is the hinge of deployable structure, which is composed of steel solid bolts and nuts and bears large gravity. Therefore, the deployable structure will be subjected to a large vertical downward force, resulting in its bending deformation. With the gradual deployment of the deployable structure, the bending deformation caused by the gravity of the hinge will become larger and larger. Therefore, the measured displacement in the X direction in the experiment is not only less than the theoretical value, but also has a larger gap; Secondly, due to the existence of machining error, the actual position, hole and rod size of the hinge on the deployable structure will not be completely consistent with the theoretical position and size, so the experimental motion trajectory of the measuring point P will be different from the theoretical motion trajectory, which may also lead to this phenomenon. In conclusion, the comparison between the experimental results and the simulation results proves that the simulation results are acceptable, which can verify the effectiveness of the novel non-locking beam element and multi-flexible body dynamic modeling method proposed in this paper.

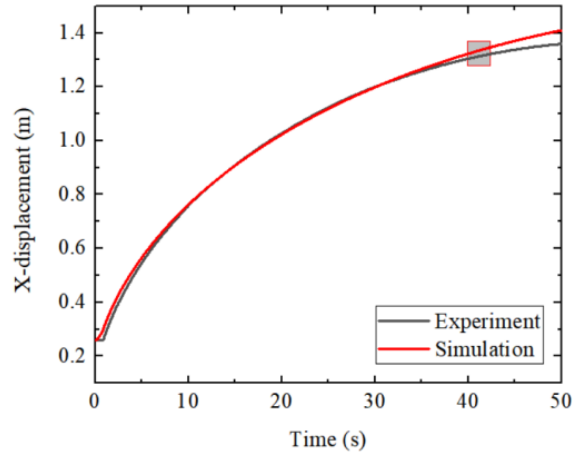

a) Displacement curve of deployable structure (overall)

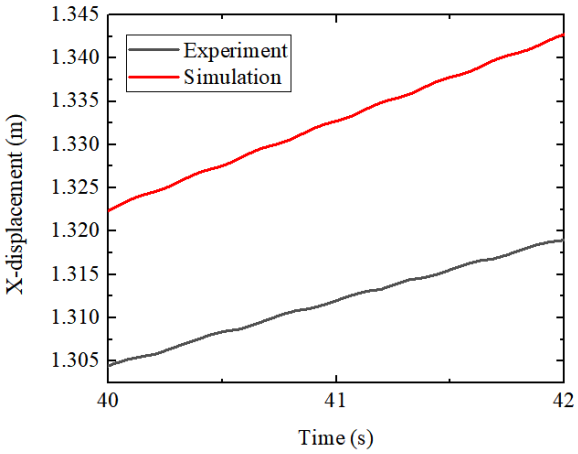

b) Displacement curve of deployable structure (local)

Fig. 20 Comparison of simulation and experimental results

8. Conclusions

Based on the absolute node coordinate method, a novel non-locking plane beam element is proposed to solve the element locking problem in the classical shear plane beam element. Through the theoretical verification of statics and dynamics, the new element can effectively avoid the three locking problems and accurately simulate the dynamic deformation of flexible components. Also, a scissor deployable structure test platform was built, and the effectiveness of the proposed new beam element and dynamic modeling method for complex mechanisms was verified by experiments. In addition, the standard matrix method is used to separate the internal node coordinates and the external constraint node coordinates of the scissor element to complete the assembly of the dynamic equations of the deployable structure, eliminate the constraint equations that need to be introduced into the dynamic equations, and convert them from differential algebraic equations to pure differential equations for easy solution.

The experimental and simulation results show that the motion of deployable structure is the coupling of large rigid body motion, small amplitude vibration and deformation during the deployment. The closer to the end, the more obvious the vibration and deformation. Therefore, the

influence of flexibility must be considered when predicting the motion law of deployable structures. This study provides a theoretical basis for the design and precise control of large deployable structures, and also provides a solution for the smooth deployment and configuration maintenance of such structures. In the follow-up study, the influence of non-smooth factors such as clearance, friction and wear on the dynamic characteristics of deployable structures will be considered, and a theoretical model containing more nonlinear factors will be established to more comprehensively and accurately simulate the motion process of the mechanism.

Acknowledgements

The authors gratefully acknowledge the financial support of the Ministry of Science and Technology "the Belt and Road" Innovative Talents Exchange Foreign Experts Project (Grant No. DL2023183003L), Natural Science Basic Research Plan in Shaanxi Province of China (Program No. 2022JM-195) and the Fundamental Research Funds for the Central Universities (Program No. G2023KY0602).

References

1. **Robert, W.** 2020. Hubble telescope 30 years in orbit: personal reflections, Research in Astronomy and Astrophysics 20(4): 1-6. http://dx.doi.org/10.1088/1674-4527/20/4/44.
2. **Roth, L.; Lvchenko, N.; Gladstone G.R.** 2021. A sublimated water atmosphere on ganymede detected from hubble space telescope observations, Nature Astronomy 5: 1043–1051. http://dx.doi.org/10.1038/s41550-021-01426-9.
3. **You, Z.; Pellegrino, S**. 1997. Cable-stiffened pantographic deployable structures part 2: mesh reflector, AIAA Journal 35(8): 813-820. https://doi.org/10.2514/2.243.
4. **Gantes, C.; Konitopoulou, E**. 2004. Geometric design of arbitrarily curved bi-stable deployable arches with discrete joint size, International Journal of Solids and Structures 41: 5517-5540. https://doi.org/10.1016/j.ijsolstr.2004.04.030.
5. **Sun, Y. T.; Wang, S. M.; Mills, J. K.; Zhi, C. J.** 2014. Kinematics and dynamics of deployable structures with scissor-like-elements based on screw theory, Chinese Journal of Mechanical Engineering 27(4): 655-662. https://doi.org/10.3901/CJME.2014.0519.098.
6. **Li, T. J; Guo. J.; Cao, Y**. 2011. Dynamic characteristics analysis of deployable space structures considering joint clearance, Acta Astronautica 68(7-8): 974-983. https://doi.org/10.1016/j.actaastro.2010.08.039.
7. **Chen, Y.; You, Z.; Tarnai, T**. 2005. Threefold-symmetric bricard linkages for deployable structures, International Journal of Solids and Structures 42(8): 2287-2301. https://doi.org/10.1016/j.ijsolstr.2004.09.014.
8. **Song, C. Y; Chen, Y.; Chen, I. M**. 2013. A 6R linkage reconfigurable between the line-symmetric bricard linkage and the Bennett linkage, Mechanism and Machine Theory 70(6): 278-292. https://doi.org/10.1016/j.mechmachtheory.2013.07.013.
9. **Moshtaghzadeh, M.; Izadpanahi, E.; Mardanpour, P.** 2021. Stability analysis of an origami helical antenna using geometrically exact fully intrinsic nonlinear composite beam theory, Engineering Structures 234(5): 111894. https://doi.org/10.1016/j.engstruct.2021.111894.
10. **Jin, Y. L.; Liu, T; Lyu, R. X; Ji, B**. 2015. Theoretical analysis and experimental investigation on buckling of FASTMast deployable structures, International Journal of Structural Stability and Dynamics 15(5): 1450075. https://doi.org/10.1142/S0219455414500758.
11. **Cai, J.; Deng, X.; Xu, Y.; Feng, J**. 2015. Geometry and Motion Analysis of Origami-Based Deployable Shelter Structures, Journal of Structural Engineering 141(10): 06015001. http://doi.org/10.1061/(ASCE)ST.1943541X.0001238.
12. **Hu, H. Y.; Tian, Q.; Zhang, W; Jin, D. P; Hu, G. K.; Song, Y. P**. 2013. Nonlinear dynamics and control of large deployable space structures composed of trusses and meshed, Advances in Mechanics 43: 390-414. http://dx.doi.org/10.6052/1000-0992-13-045.
13. **Li, J. L; Huang, H. Z; Yan, S. Z; Yang, Y. Q**. 2017. Kinematic accuracy and dynamic performance of a simple planar space deployable mechanism with joint clearance considering parameter uncertainty, Acta Astronautica 136: 34-45. https://doi.org/10.1016/j.actaastro.2017.02.027.
14. **Bai, Z. F.; Zhao, J. J**. 2020. A study on dynamic characteristics of satellite antenna system considering 3D revolute clearance joint, International Journal of Aerospace Engineering 4: 1-15. http://dx.doi.org/10.1155/2020/8846177.
15. **Li, B.; Wang, S. M; Gantes, C. G; Tan, U. X**. 2021. Nonlinear dynamic characteristics and control of planar linear array deployable structures consisting of scissor-like elements with revolute clearance joint, Advances in Structural Engineering 24(7): 1439-1455. https://doi.org/10.1177/1369433220971.
16. **Li, Y. Y.; Yang, Y.; Li, M.; Liu, Y. F.; Huang, Y. F**. 2022. Dynamics analysis and wear prediction of rigid-flexible coupling deployable solar array system with clearance joints considering solid lubrication, Mechanical Systems and Signal Processing 162(7–8): 108059. https://doi.org/10.1016/j.ymssp.2021.108059.
17. **Li, B.; Wang, S. M.; Gantes, C. J.; Tan, U. X**. 2022. Modeling and simulation for wear prediction in planar mechanical systems with multiple clearance joints, Nonlinear Dynamics 3(108): 887-910. https://doi.org/10.1007/s11071-022-07224-w.
18. **Patil, A. P.; Mishra, B. K.; Harsha, S. P**. 2021. Analytical model of rolling element bearing for studying its wear modelled as change in its clearance, Materialstoday: Proceedings 46(20): 10741-10746. https://doi.org/10.1016/j.matpr.2021.01.576.
19. **Zhu, A. B.; He, S. L.; Zou, C.; Chen, W**. 2017. The effect analysis of contact stiffness on wear of clearance joint, Journal of Tribology-Transactions of The ASME 139(3): 031403. https://doi.org/10.1115/1.4034529.
20. **Miao, H. H.; Li, B.; Liu, J.; He, A. Q.; Zhu, S. K.** 2019. Effects of revolute clearance joint on the dynamic behavior of a planar space arm system, Proceedings of the Institution of Mechanical Engineers 233(5): 1629-1644. http://dx.doi.org/10.1177/0954410018760024.
21. **Chen, X. L.; Jiang, S. Y.; Wang, T**. 2022. Dynamic modeling and analysis of multi-link mechanism considering lubrication clearance and flexible components,

Nonlinear Dynamics 107: 3365-3383.
https://doi.org/10.1007/s11071-021-07130-7.
22. **Chen, X. L.; Jiang, S. Y**. 2022. Nonlinear dynamic behavior analysis of multi-linkage mechanism with multiple lubrication clearances, European Journal of Mechanics - B/Fluids 91: 177-193.
https://doi.org/10.1016/j.euromechflu.2021.10.006.
23. **Chen, X. L.; Wang, T.; Jiang, S. Y**. 2022. Study on dynamic behavior of planar multibody system with multiple lubrication clearance joints, European Journal of Mechanics - A/Solids 91: 104404.
https://doi.org/10.1016/j.euromechsol.2021.104404.
24. **Chen, X. L.; Gao, S.; Wang, T**. 2022. Experimental verification of dynamic behavior for multi-link press mechanism with 2D revolute joint considering dry friction clearances and lubricated clearances, Nonlinear Dynamics 109: 707-729.
https://doi.org/10.1007/s11071-022-07478-4.
25. **Neto, M. A.; Ambrósio, J. A. C; Leal, R. P**. 2006. Composite materials in flexible multibody systems, Composite Methods in Applied Mechanics and Engineering 195: 6860-6873.
https://doi.org/10.1016/j.cma.2005.08.009.
26. **Zhang, Y. Q.; Duan, B. Y.; Li, T. J**. 2012. A controlled deployment method for flexible deployable space antennas, Acta Astronaut. 81(1): 19–29.
https://doi.org/10.1016/j.actaastro.2012.05.033.
27. **Shabana, A. A**. 1997. Flexible multi-body dynamics review of past and recent developments, Multibody System Dynamics 1: 189-222.
https://doi.org/10.1023/A:1009773505418.
28. **Luo, C. Q.; Sun, J. L.; Wen, H.; Jin, D. P**. 2020. Dynamics of a tethered satellite formation for space exploration modeled via ANCF, Acta Astronautica 15(177): 882-890.
https://doi.org/10.1016/j.actaastro.2019.11.028.
29. **Peng, Q. A.; Wang, S. M.; Li, B.; Zhi C. J**. 2018. Dynamics analysis of deployable structures considering a two-dimensional coupled thermo-structural effect, International Journal of Aerospace Engineering 1752815.
https://doi.org/10.1155/2018/1752815.
30. **Otsuka, K.; Makihara, K**. 2019. Absolute nodal coordinate beam element for modeling flexible and deployable aerospace structures, AIAA Journal 57(3): 1343-1346.
https://doi.org/10.2514/1.J057780
31. **Ghorbani, H.; Tarvirdizadeh, B.; Alipour, K.** 2019. Near-time-optimal motion control for flexible-link systems using absolute nodal coordinates formulation, Mechanism and Machine Theory 140:686-710.
https://doi.org/10.1016/j.mechmachtheory.2019.06.032.
32. **Daniel, G. V.; Mikkola, A. M.; José-Luis, Escalona**. 2007. A new locking-free shear deformable finite element based on absolute nodal coordinates, Nonlinear Dynamics 50(1-2): 249-264.
https://doi.org/10.1007/s11071-006-9155-4.
33. **Gerstmayr. J.; Sugiyama, H.; Mikkola, A**. 2013. Review on the absolute nodal coordinate formulation for large deformation analysis of multibody Systems, Journal of Computational and Nonlinear Dynamics 8: 031016-1.
http://doi.org/10.1115/1.4023487.
34. **Gerstmayr, J.; Shabana, A. A**. 2006. Analysis of thin beams and cables using the absolute nodal co-ordinate formulation, Nonlinear Dynamics 109-130.
https://doi.org/10.1007/s11071-006-1856-1.
35. **Shabana, A. A**. 2015. Definition of ANCF finite elements, Journal of Computational and Nonlinear Dynamics 10(5): 054506.
https://doi.org/10.1115/1.4030369.
36. **Li, T. J.; Wang, Y**. 2009. Deployment dynamic analysis of deployable antennas considering thermal effect, Aerospace Science & Technology 13(4-5): 210-215.
https://doi.org/10.1016/j.ast.2009.04.005.
37. **Omar. M.A.; Shabana, A.A**. 2001. A two-dimensional shear deformable beam for large rotation and deformation problems, Journal of Sound & Vibration 243(3):565-576.
https://doi.org/10.1006/jsvi.2000.3416.

B. Li, Qi'an Peng, S. Wang, J. Zhu, Gantes J. Charis

MODELING AND ANALYSIS OF FLEXIBLE DEPLOYABLE STRUCTURE WITH SCISSOR-LIKE ELEMENTS USING A NOVEL NON-LOCKING BEAM ELEMENT

S u m m a r y

The main goal of this paper is to develop a comprehensive dynamic modeling and analysis method based on the absolute node coordinate method to predict the impact of the member flexibility on the dynamic performance of scissor deployable structure under the framework of flexible multi-body dynamics. In the process, three locking problems in the classical plane shear beam element are reviewed and discussed. Then a novel non-locking planar beam element is proposed to solve the element locking problem, and the dynamic model of the scissor deployable structure is established. Next, the cantilever beam, simply supported beam and flexible simple pendulum are respectively used to verify the correctness of the proposed non-locking beam element from the static and dynamic perspectives. Finally, the simulation and experiment results show that the proposed new non-locking element and normal matrix modeling method can effectively evaluate the dynamic performance of deployable structure and improve the computational efficiency. This study not only provides theoretical guidance for the dynamic behavior analysis and prediction of scissor deployable structure, but also offers reference for the layout and design of same type mechanisms.

Keywords: deployable structure, non-locking element, dynamic analysis, modeling, simulation.

Received March 14, 2023
Accepted December 3, 2023